Characterizing nuclear morphology and expression of eNOS in vascular endothelial cells subjected to a continuous range of wall shear stress magnitudes and directionality

Jaideep Sahni[1], Mehwish Arshad[2], Morgan A. Schake[1], Justin R. Brooks[1], Ruiguo Yang[1], Peter D. Weinberg[2], Ryan M. Pedrigi[1]

[1]Department of Mechanical and Materials Engineering, University of Nebraska-Lincoln, USA

[2]Department of Bioengineering, Imperial College London, UK

Correspondence:

Ryan M. Pedrigi, Ph.D.

Mechanical and Materials Engineering

University of Nebraska-Lincoln

Nebraska Hall

P.0. Box 880526

Lincoln, NE 68588-0526

P: (402) 472-2732

F: (402) 472-8292

E: rpedrigi@unl.edu

Keywords: endothelium, nuclear area, nuclear aspect ratio, endothelial nitric oxide synthase, Kruppel-like factor 2, hemodynamics, mechanical dose response, mechanobiology

Abstract

Complex patterns of hemodynamic wall shear stress occur in regions of arterial branching and curvature. Areas within these regions can be highly susceptible to atherosclerosis. Although many studies have characterized the response of vascular endothelial cells to shear stress in a categorical manner, our study herein addresses the need of characterizing endothelial behaviors over a continuous range of shear stress conditions that reflect the extensive variations seen in the vasculature. We evaluated the response of human umbilical vein endothelial cell monolayers to orbital flow at 120, 250, and 350 revolutions per minute (RPM) for 24 and 72 h. The orbital shaker model uniquely provides a continuous range of shear stress conditions from low and multidirectional at the center of each well of a culture plate to high and unidirectional at the periphery. We found distinct patterns of endothelial nuclear area, nuclear major and minor diameters, nuclear aspect ratio, and expression of endothelial nitric oxide synthase over this range of shear conditions and relationships were fit with linear and, where appropriate, power functions. Nuclear area was particularly sensitive with increases in the low and multidirectional WSS region that incrementally decreased as WSS became higher in magnitude and more unidirectional over the radius of the cell layers. The patterns of all endothelial behaviors exhibited high correlations (positive and negative) with metrics of shear stress magnitude and directionality that have been shown to strongly associate with atherosclerosis. Our findings demonstrate the exquisite sensitivity of these endothelial behaviors to incremental changes in shear stress magnitude and directionality, and provide critical quantitation of these relationships for predicting the susceptibility of an arterial segment to diseases such as atherosclerosis, particularly within complex flow environments in the vasculature such as around bifurcations.

1. Introduction

Vascular endothelial cells form the inner lining of arteries and are exquisitely sensitive to the blood flow environment (Frueh et al., 2013). The flow of blood through the artery exerts a tangential mechanical load on the endothelium called a shear stress that has been shown to be an important regulator of phenotype (Davies et al., 2013). Wall shear stress (WSS) resulting from normal blood flow (i.e., flow along parallel streamlines at a physiologic mean velocity) promotes elongation of endothelial cells and their nuclei (Arshad et al., 2021), as well as the principal functions of a normal (healthy) phenotype, including regulation of vasodilation (Noris et al., 1995), anticoagulation properties (Frangos et al., 1985), the barrier function (Walsh et al., 2011), and anti-inflammatory properties (Hosoya et al., 2005). Conversely, WSS resulting from so-called disturbed blood flow, which has a low magnitude and/or changing direction over the cardiac cycle, can disrupt these functions of the endothelium. Segments of large arteries around bifurcations and areas of high curvature, where disturbed blood flow is naturally present, contain a dysfunctional endothelium that is primed for the development of diseases such as atherosclerosis (Davies et al., 2013). Importantly, although arterial regions with bifurcations and curvature contain disturbed blood flow, they also contain normal flow. For example, flow near the inner curvature of a bend is low and multidirectional whereas flow near the outer portion is high and unidirectional. Thus, there is a continuous range of flow conditions in these vessel segments that promote both functional and dysfunctional endothelial phenotypes.

The same WSS magnitudes and directionality that determine the balance between a functional and dysfunctional endothelium are also strongly associated with the initiation and progression of atherosclerosis. Although many *in vitro* and *in vivo* studies have quantified these associations, virtually all of them do so with a categorical approach. For example, *in vitro* studies have demonstrated that shear stress induces changes in endothelial nuclear morphology (Anno et al., 2012; Bond et al., 2010; Danielsson et al., 2022), which may play an important role in mechanotransduction by causing: adaptations of nuclear envelope structures (Danielsson et al., 2022), activation of stretch-sensitive ion channels on the nuclear membrane (Fedorchak et al., 2014), altered interactions with transcription factors (Mammoto et al., 2012), changes in the position of genes within the nucleus (Fedorchak et al., 2014), and direct conformational changes in the DNA structure (Anno et al., 2012). However, these and other comparable studies only evaluated three or fewer shear stress conditions, such as static control, low WSS (or otherwise disturbed; for example, oscillatory WSS), and normal WSS. Similarly, while numerous studies have investigated the flow-sensitive nature of endothelial nitric oxide synthase (eNOS), the

precursor to NO and an important marker of endothelial function, virtually all of them performed these studies using the same three or fewer shear stress conditions (Duerrschmidt et al., 2006; Jin et al., 2021; Rizzo et al., 2003; Siu et al., 2016; Warboys et al., 2014; Won et al., 2007). This approach is consistent for nearly all *in vitro* studies evaluating endothelial behaviors under flow. Likewise, *in vivo* studies of the mechanobiology of atherosclerosis that have examined the association between local arterial regions of plaque development and the presence of certain WSS conditions, which are most often characterized by WSS metrics, also tend to group these conditions into three or fewer categories (Cheng et al., 2006; Samady et al., 2011; Stone et al., 2012), even though computational fluid dynamics is used to compute WSS over a continuous range at each point in the artery. While this categorical approach serves as an important tool that has uncovered many significant relationships between WSS, endothelial function, and atherosclerosis, there remains a need to quantify these relationships over a continuous range of WSS conditions (Humphrey, 2008). In particular, characterization of endothelial behaviors over a range of shear stresses that are representative of the complex flow conditions present in arterial regions around bifurcations and high curvature are critical for better understanding how incremental changes in shear stress affect endothelial function and, in turn, the susceptibility of an arterial segment to atherosclerosis initiation and progression to advanced plaque phenotypes. These data are also important for the improvement of multiscale models attempting to predict endothelial function and atherogenesis. They also allow quantification of metrics, such as correlation coefficients, that give insights into the predictive capability of mechanical biomarkers that cannot be obtained from categorical associations.

Therefore, in this study, we quantified two fundamental behaviors of vascular endothelial cells under flow, changes in nuclear morphology and expression of eNOS, over a continuous range of WSS conditions from low and multidirectional to high and unidirectional. We also demonstrate high correlations between these two behaviors and several WSS metrics that have previously been shown to strongly associate with atherogenesis. To do this, we used an orbital shaker model that uniquely provides this range of flow conditions from the center of each well of a culture plate to the periphery (Ghim et al., 2018; Warboys et al., 2019). We performed these experiments using human umbilical vein endothelial cell (HUVEC) layers seeded into 6-well culture plates and placed atop an orbital shaker for durations of 24 and 72 h. Finally, we also compared the expression of several atheroprotective and atherogenic genes at the center versus periphery of other endothelial cell layers subjected to orbital flow to further characterize endothelial phenotype in these two distinct regions.

2. Materials and Methods

2.1. Cell culture and application of orbital flow

HUVECs pooled from 10 donors (ATCC) were used for all experiments at passages 4 to 7. A recent study comparing HUVECs to human aortic endothelial cells demonstrated very similar differential gene expression when exposed to disturbed versus laminar shear stress for several functional-relevant genes, including some of those used herein (e.g., KLF2 and eNOS) (Maurya et al., 2021). Also, obtaining vascular endothelial cells from pooled donors reduced the biological variability that can exist between donors.

Cells were maintained with vascular cell basal medium, supplemented with endothelial cell growth kit-BBE (ATCC) and 0.1% Penicillin-Streptomycin-Amphotericin B Solution (ATCC) within a humidified incubator at 37°C and 5% CO_2, as per the supplier's protocol. For experiments, cells were seeded into 6-well glass-bottomed culture plates (Cellvis) coated with rat tail type I collagen (Corning) at a density of 40,000 cells/cm^2 (the density at confluence). Cells were visually inspected with a light microscope immediately before and after each experiment to ensure confluence and a healthy appearance (Figures A.1 and A.2, Appendix A). Experiments were run one day after seeding with 2.41 ml of media per well to give an average medium height of 2.5 mm. In each experiment, well plates were either subjected to orbital flow or maintained under static conditions, as a control, for 24 or 72 h. Control cell layers were seeded at the same time as cell layers exposed to orbital flow for every experiment. Orbital flow was induced by placing the well plate atop an orbital shaker (Grant Instruments), which moves the plate in a planar circular orbit of 5 mm radius, and rotating it at 120, 250, or 350 RPM within a humidified incubator at 37°C and 5% CO_2.

2.2. Immunostaining, imaging, and analysis

After exposure to orbital flow, cells were immediately covered with 4% paraformaldehyde in PBS for 10 mins and then stained for nuclei and eNOS. Briefly, cells were permeabilized with 0.1% Triton X100 in PBS for 15 mins and incubated with blocking buffer (1% w/v bovine serum albumin, 22.52 mg/ml glycine, in PBST) for 30 mins to prevent nonspecific binding. Cell layers were then incubated with mouse anti-eNOS primary antibody (ab76198, Abcam) at 1:100 overnight at 4˚C and Alexa Fluor 488-labelled secondary antibody (ab150117, Abcam) at 1:700 for 1 h at room temperature. Cells were incubated with 10 μM DAPI counterstain (ab228549, Abcam) for 2 min. All antibodies were diluted in blocking buffer and incubation steps were conducted on a rocker for even distribution.

After staining, cell layers were imaged with a Zeiss LSM 800 confocal microscope using a 10x objective. The eNOS stain was excited at 488 nm and its emission was recorded at 489-585 nm, whereas DAPI was excited at 405 nm and its emission was recorded at 406-500 nm. All confocal settings were kept constant over all cell layers. A tile scan of 30x2 TIFF images, each with 1024x1024 pixels, was taken to capture the cells from the center to the periphery of each well (the outer edge of the last image taken was ~0.5 mm from the wall of the well). Data reduction was performed for both nuclear morphology (from DAPI) and eNOS by averaging the imaging data over the two rows (to create a 30x1) and then over sets of four images along the radius of each well, excluding the ends (center and periphery), which were not averaged with surrounding images. This created a final data matrix of 9x1. The locations of these data points are 0, 1.4, 3.7, 6.0, 8.3, 10.6, 12.9, 15.2, and 16.7 mm from the center of the well. The endpoints (0 and 16.7 mm) are each from a single image so represent the data in a radial span of ±0.3 mm, whereas the other points represent data from four images which equates to a radial span of ±1.2 mm. This final data matrix for each data set was used for all immunostaining–related analyses. For statistical comparisons over the well radius, the central one third of the radius of each cell layer (first three data points) and, separately, peripheral one third of the radius of each cell layer (last three data points) were averaged and used to compare each orbital velocity to static controls.

Images of the DAPI stain were automatically processed to quantify nuclear area, major diameter, minor diameter, and aspect ratio using a custom script in ImageJ (Schneider et al., 2012). The major and minor diameters were obtained by ImageJ using a best-fit ellipse and the ratio of these diameters was taken as the aspect ratio. This script also employed a color threshold to identify nuclei and removed any nuclei that were outside of a prescribed range of pixel areas of 300 to 800 pixels and circularity of 0.6 to 1.0 (determined manually, to avoid counting clustered nuclei). In a typical 10x image, these metrics of nuclear morphology were obtained from over 200 nuclei. To acquire an accurate estimate of the number of cells per image, DAPI images were also processed using a custom program in MATLAB. These images were binarized (i.e., pixels within the nuclei were assigned a value of 1 and pixels outside of nuclei were assigned a value of 0), followed by morphological closing to remove holes in the DAPI signal and then an operation was performed to remove objects (i.e., noise) below a threshold pixel area that was determined manually (and held constant for all images). The DAPI-positive pixels were then summed over each image and divided by the mean number of pixels per nucleus (i.e., nuclear area) for that image obtained from ImageJ to estimate the number of cells in the image. This approach avoids the artifacts resulting from nuclei that are clustered or only partially visible at the image periphery. The intensity of the eNOS stain within each image was also quantified using this MATLAB

program by converting these images to greyscale and summing the pixel values (which ranged from 0 to 255) over the entire image. For each image, the sum of eNOS intensity was normalized by the number of cells to obtain the average eNOS per cell. Finally, both nuclear area and eNOS at each radial location of all cell layers are reported relative to their average value at each radial location of the static controls seeded at the time of each experiment. The individual controls are also divided by their mean to show variability and they are pooled together from all experiments for statistical comparisons. This approach accounts for slight variabilities due to spatial position within each well, passages, and cell lines. For completeness, each biological readout as a function of well position is also given in absolute units in Appendix B.

2.3. RT-qPCR

RT-qPCR was used to evaluate the expression of three atheroprotective genes and three atherogenic genes to substantiate the immunochemistry findings of different endothelial behaviors in the low and multidirectional WSS region versus the high and unidirectional WSS region under orbital flow. The atheroprotective genes were eNOS, thrombomodulin (*THBD*), and Kruppel-like factor-2 (*KLF-2*), whereas the atherogenic genes were endothelin-1 (*ET-1*), connective tissue growth factor (*CTGF*), and caveolin-1 (*CAV1*). These genes were chosen because they are important markers of endothelial function and have been shown to be highly sensitive to shear stress (Fledderus et al., 2008; Frueh et al., 2013; McCormick et al., 2001; Peghaire et al., 2019). At the end of each experiment, total ribonucleic acid (RNA) was obtained from cell layers at both the inner portion of the well ($<$9 mm radius) and the outer portion of the well (11.8-17.4 mm radially from the center). To do this, we designed a custom device that contained six masks, one for each well, and fabricated it using a 3-D printer (Stratasys Objet 500 Connex3 3D printer) (Figure 1).

The device was printed with VeroClear™ and each mask had a channel at the bottom that was fitted with a silicone gasket (McMaster-Carr) to create a seal with the bottom of the culture plate. This seal was improved by tightening screws on the outer portion of the device to a base plate. Using this device, cells from each region of each well of the culture plate were lysed with RLT cell lysis buffer (QIAGEN) and vortexed for 30 seconds. RNA was isolated using an RNeasy Micro Kit (QIAGEN). mRNA quality was assessed by measuring the 260/280 absorbance with a Take3 plate on a Cytation 5 plate reader (BioTek); ratios between 1.95 and 2.05 indicated an acceptable purity (Okamoto and Okabe, 2000). Reverse transcription (RT) was done with an iScript kit (Bio-Rad) converting 800 ng of RNA with a MiniAmp Thermal Cycler (Applied Biosystems). Primers were designed (Table A.1, Appendix A) and efficiencies tested with loading

conditions from 500 pg/µl to 500 fg/µl of cDNA, assuming a 1:1 RT conversion from RNA, where efficiencies between 90-110% were considered acceptable. PCR was run following the manufactures protocol, with 40 pg/µl in triplicate with SsoAdvanced Universal SYBR® Green Supermix (Bio-Rad) using a QuantStudio 3 Real-Time PCR System (Applied Biosystems).

Data were analyzed with the delta-delta Ct method. Briefly, this approach computes the amount of gene expression by normalizing to a reference gene, HPRT-1 (ΔCt), and then taking the difference in this value relative to the mean ΔCt value of the static control cell layers (ΔΔCt). The negative of this final value is then taken as the exponent to base 2 ($2^{-\Delta\Delta Ct}$) to express fold changes in expression. Note that the reference is 1 (i.e., $2^0 = 1$).

2.4. Computational fluid dynamics and wall shear stress metrics

These methods have been described previously (Ghim et al., 2018). Briefly, the commercial computational fluid dynamics (CFD) package Star CCM+ (version 11.02.009, CD-Adapco, USA) was used for all flow simulations. A single well of a 6-well plate was represented as a cylinder with a height of 10 mm and radius of 17.4 mm. The culture medium had a height of 2.5 mm at rest and the remaining space was filled with air. The geometry was discretized using a structured cylindrical mesh with 360,000 grid elements. The explicit unsteady model was used. A no-slip condition was imposed at all walls and surface tension was neglected. The top surface of the cylinder was defined as a pressure outlet. The dynamic viscosity and density of the medium were 0.78 mPa.s and 1003 kg/m^3, respectively, whereas the dynamic viscosity and density of air were 0.0187 mPa.s and 1.1115 kg/m^3. The rotation of the well was modelled by introducing an acceleration given by:

$$[A\omega^2 \cos(\omega t), A\omega^2 \sin(\omega t), -9.81] \quad (1)$$

where A is the orbital radius of the shaker, ω is the angular velocity, and t is time. All three orbital velocities used in the cell experiments were simulated: 120, 250, and 350 RPM (Figure 2A). These were chosen to provide a broad physiologic range of WSS conditions; for example, the maximum time-averaged WSS (TAWSS) over the three orbital velocities was 0.48, 1.89, and 2.97 Pa, respectively, which represents low, average (or normal), and moderately high values in human arteries (Gijsen et al., 2019). The primary output was the instantaneous WSS vector at each element on the base of the well at each time increment over one complete revolution. Maximum WSS was used to assess convergence. A mesh independence study was performed using 720,000 grid elements, and no difference was observed.

The instantaneous WSS vectors were used to calculate four WSS metrics using a custom program in MATLAB, as previously described (Arshad et al., 2021). Two of these WSS metrics related to magnitude, TAWSS and the magnitude of the mean WSS (MagMeanWSS), and two of them related to directionality, the oscillatory shear index (OSI) and the transverse WSS (TransWSS) (Figure 2B-E). TAWSS is the average of the magnitudes of the instantaneous WSS vectors over one cycle of the shaker, while MagMeanWSS is the magnitude of the average WSS vector over one cycle. OSI quantifies the instantaneous WSS vectors that do not align with the mean WSS vector, which includes the degree of back-and-forth (uniaxial) flow, over one cycle, while TransWSS is the magnitude of the components of the instantaneous WSS vectors that are perpendicular to the mean WSS direction, averaged over one cycle (Ghim et al., 2018). Since TransWSS does not quantify uniaxial oscillatory flow, it is complementary to OSI.

2.5. Statistics and Curve Fitting

All statistical tests were performed in Minitab. Quantities are reported as mean ± standard deviation (SD). If the data were normally distributed (determined by a Shapiro-Wilks test), group comparisons were performed using a one-way analysis of variance (ANOVA) and pairwise comparisons, including those post-hoc of the ANOVA, were performed using a two-tailed *t*-test. Otherwise, a Kruskill-Wallis test (group comparisons) and Mann-Whitney U test (pairwise comparisons) were used. For these tests, multiple comparisons were accounted for using a Bonferroni-Holm correction method. To quantify trends in the mechanical dose-response curves (i.e., each endothelial behavior as a function of each WSS metric), data were fit to a line and, where applicable, a power function using a linear and nonlinear regression, respectively, in MATLAB. The linear and power functions are given as

$$EC\ Behavior = a * (WSS\ metric) + b \quad (1)$$

and

$$EC\ Behavior = a * (WSS\ metric)^b + c \quad (2)$$

, respectively, where ***a***, ***b***, and ***c*** are the constants being fit by regression (reported in Table A.2 and A.3). A Spearman's rank correlation coefficient (ρ) was also computed to quantify the strength of the linear relationship. The qualitative interpretation of the calculated coefficient (e.g., very high, high, moderate, etc.) was done following previous work (Mukaka, 2012). For correlations, multiple comparisons were accounted for using a Bonferroni correction method. All corrections for multiple comparisons were implemented as an adjustment of the calculated *p*-value via multiplying by the

ratio of 0.05 to the adjusted alpha value. An adjusted *p*-value of less than 0.05 was considered statistically significant, which is indicated as *$p<0.05$, **$p<0.01$, ***$p<0.001$, and ****$p<0.0001$.

3. Results

3.1. Endothelial nuclear morphology as a function of wall shear stress condition

Endothelial nuclear area and aspect ratio was highly dependent on the angular velocity of the orbital shaker (Figure 3). At 24 h, nuclear area (relative to controls) in the central one third (of the radius) of cell layers exhibited no significant difference from controls (1.00±0.02) at either 120 or 250 RPM, but in the peripheral one third (of the radius) of cell layers nuclear area was significantly decreased from controls (1.00±0.01) under all three orbital velocities with values of 0.94±0.02 at 120 RPM ($p=0.0002$), 0.89±0.03 at 250 RPM ($p=0.0004$), and 0.85±0.01 at 350 RPM ($p<0.0001$) (Figure 3B). Note that 350 RPM could only be assessed at the periphery of cell layers due to the central portion being nearly devoid of medium (i.e., centrifugal forces pushed the medium to the periphery). At 72 h, there were significant changes in both the central and peripheral regions of cell layers subjected to orbital flow. In the central one third of cell layers, nuclear area significantly increased from controls (1.00±0.03) with values of 1.03±0.01 at 120 RPM ($p=0.03$) and 1.05±0.02 at 250 RPM ($p=0.004$). In the peripheral one third of cell layers, nuclear area significantly decreased from controls (1.00±0.02) with values of 0.95±0.02 at 120 RPM ($p=0.0007$), 0.94±0.01 at 250 RPM ($p<0.0001$), and 0.90±0.01 at 350 RPM ($p<0.0001$) (Figure 3C).

The nuclear aspect ratio at these angular velocities showed a roughly inverse trend to area (note that aspect ratios are reported as raw values, not relative to controls). At 24 h, there was no statistical difference in the mean aspect ratio between any of the cell layers under orbital flow versus static controls, except at 350 RPM, where nuclear aspect ratios were statistically lower (Figure 3D). At 72 h, the central one third of cell layers under 250 RPM exhibited an aspect ratio of 1.51±0.01, which was statistically lower than that seen in control cell layers of 1.54±0.01 ($p=0.005$). The peripheral one third of cell layers at both 250 and 350 RPM also showed statistical differences from control cell layers with increased aspect ratios of 1.62±0.02 ($p<0.0001$) and 1.68±0.02 ($p<0.0001$), respectively, versus 1.55±0.02 in controls (Figure 3E).

We also evaluated nuclear major and minor diameters to better understand the changes in nuclear area and aspect ratio over time. Interestingly, the major diameter exhibited the same shortening trends across the three orbital velocities as nuclear area at 24 h, but then re-elongated

at 72 h, whereas the minor diameter exhibited a similar degree of shortening between 24 h and 72 h (Figure 4). This explains why the nuclear aspect ratio was only significantly increased at the periphery of cell layers under 250 and 350 RPM at 24 h, but not 72 h, despite clear changes (decreases) in nuclear area at 24 h. Note that nuclear area, major diameter, and minor diameter all showed nearly identical trends when evaluated in absolute units (Figure B.1, Appendix B).

We next evaluated how shear stress magnitude and directionality separately associated with nuclear area and aspect ratio. Nuclear area exhibited strong correlations with some of the WSS metrics. TAWSS showed moderate negative correlations with nuclear area of -0.60 at 24 h (p=0.02) and -0.48 at 72 h (p=0.12) (Figure 5A-B), while MagMeanWSS exhibited high negative correlations of -0.83 at 24 h (p<0.0001) and -0.74 at 72 h (p=0.0007) (Figure 5C-D). Both metrics appeared to exhibit a nonlinear relationship with nuclear area that was better fit with a power function. OSI also exhibited strong correlations with nuclear area with a high positive correlation of 0.88 at 24 h (p<0.0001) and 0.80 at 72 h (p<0.0001) (Figure 5E-F). TransWSS over the radius of each culture plate well was inconsistent between orbital velocities, so did not allow for meaningful evaluation of correlations when all orbital velocities were combined (Figure B.2). Thus, we evaluated the correlation between nuclear area and this metric at 250 RPM only. At this orbital velocity, TransWSS exhibited similar patterns as OSI with a very high positive correlation of 0.97 at 24 h (p=0.0002) and a high correlation of 0.80 at 72 h (p=0.01) (Figure 5G-H). Similar correlative trends were observed with the nuclear major and minor diameters, although the minor diameter had the strongest trends, particularly at 72 h where the major diameter re-elongated towards values seen in the controls and thus lost significant correlations with the shear metrics (Figures B.3-B.4).

Nuclear aspect ratio exhibited strong correlations with the WSS metrics at 72 h, but not 24 h (Figure 6). Because cells exposed to 120 RPM exhibited no statistical difference in nuclear aspect ratio from controls at any point along the radius of the cell layers, these data were removed from the correlation calculations. Nuclear aspect ratio in the remaining cell layers at 72 h exhibited a high positive correlation with TAWSS (ρ=0.83, p=0.007) (Figure 6B), a very high positive correlation with MagMeanWSS (ρ=0.90, p<0.0001) (Figure 6D), a high negative correlation with OSI (ρ=-0.81, p=0.009) (Figure 6F), and a high negative correlation with TransWSS at 250 RPM (ρ=-0.87, p=0.005) (Figure 6H).

3.2. Endothelial expression of eNOS as a function of wall shear stress condition

Endothelial expression of eNOS was also dependent on the angular velocity of the orbital shaker (Figure 7). Quantifying the fluorescence intensity relative to the mean eNOS expression of the static condition (control) at 24 h demonstrated no statistical difference between either orbital velocity over the central one third of cell layers, where disturbed flow is present. At 120 RPM, cells exhibited no significant change in eNOS across the entire radius of the cell layers (mean eNOS was 0.95±0.21 versus 1.00±0.15 in the controls). In contrast, the peripheral one third of cell layers under 250 and 350 RPM demonstrated significantly increased eNOS expression with mean values of 1.85±0.32 (p=0.002) and 2.19±0.15 (p<0.0001), respectively (Figure 7B). The trends at 72 h were very similar to 24 h, although eNOS in the central one third of cell layers at 250 RPM was significantly elevated compared to controls with a mean value of 1.24±0.11 versus 1.00±0.18 (p=0.02). In the peripheral one third of cell layers, eNOS expression significantly increased to 1.49±0.15 (p=0.0004) and 2.49±0.08 (p=0.009) at 250 and 350 RPM, respectively (Figure 7C). Interestingly, in this region, cell layers under 120 RPM exhibited a decrease in eNOS with a mean value of 0.84±0.16, although this value was not significantly different from the controls (p=0.09). eNOS showed nearly identical trends when plotted in absolute units (Figure B.5).

The expression of eNOS also correlated well with the shear metrics. TAWSS showed a very high positive correlation with eNOS of 0.86 at 24 h (p<0.0001) and a high correlation of 0.76 at 72 h (p=0.0003) (Figure 8A-B). MagMeanWSS also showed a high positive correlation with eNOS of 0.72 at 24 h (p=0.001), but only a low (non-significant) correlation of 0.48 at 72 h (p=0.12) (Figure 8C-D). The two WSS metrics of directionality, OSI and TransWSS, also showed significant correlations with eNOS at 24 h, but not 72 h. OSI showed a moderate negative correlation with eNOS of -0.59 at 24 h (p=0.02), but a low (non-significant) negative correlation of -0.33 at 72 h (p=0.58) (Figure 8E-F). Interestingly, OSI also exhibited a clear nonlinear relationship with eNOS that was well fit with a power function. TransWSS at 250 RPM exhibited a very similar trend with eNOS as OSI with a high negative correlation of -0.72 at 24 h (p=0.04) and a low (non-significant) negative correlation of -0.37 at 72 h (p=0.34) (Figure 8G-H).

The correlation analysis was also done for nuclear area, nuclear aspect ratio, and eNOS using the data from 250 RPM only (Figures B.6-B.8).

3.3. Changes in endothelial gene expression between the low and multidirectional compared to high and unidirectional wall shear stress conditions

We also performed RT-qPCR to assess the expression of three atheroprotective genes, including the gene that codes for eNOS, and three atherogenic genes. The expression of each gene was normalized by one housekeeping gene (*HPRT-1*) and reported relative to the static condition (using the $2^{-\Delta\Delta Ct}$ method) for endothelial cell layers exposed to orbital flow at 120 and 250 RPM for both durations, 24 and 72 h. Gene expression was evaluated at the center and periphery of the cell layers to better characterize endothelial phenotype under the different flow conditions in these two regions (Figure 9A). At 250 RPM for 24 h, there was a statistically significant increase in *eNOS* (2.02±0.40 versus 4.93±1.18, p=0.01), *THBD* (4.88±1.57 versus 22.16±5.2, p=0.01), and *KLF-2* (10.38±2.25 versus 22.95±4.80, p=0.01) from the center to the periphery of the cell layers, while there was a significant decrease in *ET-1* (1.66±0.67 versus 0.24±0.09, p=0.02), *CTGF* (1.10±0.26 versus 0.36±0.11, p=0.01), and *CAV1* (1.08±0.19 versus 0.72±0.06, p=0.02) (Figure 9B). Similar results were seen at 250 RPM for 72 h (Figure 9C). In contrast, endothelial cells exposed to orbital flow at 120 RPM for 24 h showed no significant differences in the expression of any genes at the center versus periphery (Figure 9D). At 72 h, all three atherogenic genes were statistically higher at the center versus the periphery of the cell layers: *ET-1* (1.45±0.17 versus 0.49±0.16, p=0.0002), *CTGF* (1.26±0.26 versus 0.47±0.15, p=0.04), and *CAV1* (1.59±0.26 versus 0.67±0.21, p=0.002) (Figure 9E).

4. Discussion

In this study, we evaluated nuclear morphology and eNOS expression within endothelial cell layers over a range of WSS from low and multidirectional to high and unidirectional using an established orbital shaker model (Ghim et al., 2018; Warboys et al., 2019). To our knowledge, this study is the first to characterize changes in these fundamental endothelial behaviors over a range of WSS conditions that are similar to those found around bifurcations and the inner curvature of highly curving arteries, including with a similar range of WSS magnitudes (e.g., TAWSS ranged from 0.07 to 3 Pa) and directionality (e.g., OSI ranged from 0.01 to 0.5). We also demonstrated high correlations (positive and negative) between these endothelial behaviors and WSS metrics of magnitude and directionality, which indicated a strong ability of these metrics to predict endothelial function. The best-fit parameters for linear and, in some cases, nonlinear (power) functions were also reported to quantify these mechanical dose response curves, which can be used in models of endothelial function. Although all endothelial behaviors exhibited strong

associations with WSS, nuclear area exhibited particularly exquisite sensitivity with incremental increases from controls in the low and multidirectional WSS region and decreases in a stepwise fashion as WSS became higher in magnitude and more unidirectional over the radius of the culture plate wells. While these changes were subtle, they were clearly distinct with very low standard deviations (<4% of the mean). Interestingly, nuclear aspect ratio showed no significant increases from controls at 24 h, despite changes in nuclear area, whereas at 72 h cell layers under both 250 and 350 RPM exhibited significant increases. This result stemmed from similar changes in the major and minor diameters of the nuclei at 24 h, causing no change in aspect ratio, but a recovery of the major diameter at 72 h while the minor diameter remained shortened. These differences over time suggest that the endothelial cells had not fully adapted to the flow by 24 h. If reorientation was incomplete, the cells would have experienced WSS at a different angle relative to their long axis at 24 h versus 72 h, which may explain the small differences in eNOS protein expression, nuclear area, and gene expression observed between the two time points.

Endothelial expression of eNOS also exhibited strong sensitivity to WSS and high correlations with the WSS metrics, though it did not appear to be as sensitive as nuclear area, particularly at 120 RPM where little change was observed over the radius of the culture plate wells. Interestingly, eNOS appeared unresponsive to changes in OSI at 120 RPM (i.e., it did not exhibit the inverse relationship seen at higher orbital velocities), which suggests that WSS directionality may not influence this principal endothelial function below a certain threshold of magnitude (the maximum TAWSS at 120 RPM was 0.48 Pa). This finding aligns with our RT-qPCR data at 120 RPM showing no differences in the expression of atheroprotective genes at the periphery versus the center of endothelial cell layers at either time point (only the atherogenic genes were statistically different at 72 h). In contrast to 120 RPM, endothelial cell layers exposed to 250 RPM exhibited distinct phenotypes at the periphery versus the center with significant increases in the atheroprotective genes and decreases in the atherogenic genes.

These findings of high correlations between markers of endothelial function (eNOS and nuclear morphology) and WSS metrics demonstrate the sensitivity of the endothelium to incremental changes in WSS over a range of conditions, which may be leveraged to aid in predicting arterial function and dysfunction. In addition, these findings suggest that the susceptibility of an arterial segment to atherosclerosis has a similar level of high sensitivity to the blood flow condition that may be important in determining, not just initiation, but also progression to different plaque phenotypes. Indeed, studies in patients have demonstrated strong associations between different plaque types and WSS conditions, including low WSS magnitude (Stone et al.,

2018; Stone et al., 2012) and high changes in WSS direction over the cardiac cycle (Kok et al., 2019; Timmins et al., 2017). These same WSS conditions have also been shown to associate with the development of atherosclerosis in hypercholesterolemic animal models (Chatzizisis et al., 2011; Hoogendoorn et al., 2020; Mohamied et al., 2015; Peiffer et al., 2013), including those that have been instrumented with a blood flow-modifying device around or within a target artery (e.g., carotid and coronary arteries) to demonstrate causal relationships between WSS conditions and atherosclerosis initiation and progression to different plaque types (Cheng et al., 2006; Miller et al., 2021; Pedrigi et al., 2016; Pedrigi et al., 2015). Despite these strong associations reported previously, there is a need to continue to refine our understanding of these relationships for the further development of reliable prognostic indictors of plaque progression and models seeking to predict such pathological processes. Quantifying endothelial behaviors over a range of shear stress conditions is an important aspect of improving such predictive tools.

CRediT authorship contribution statement

Jaideep Sahni: Methodology, Validation, Formal analysis, Investigation, Data curation, Writing – original draft, Writing – review & editing, Visualization. **Mehwish Arshad**: Methodology, Software, Validation, Investigation, Writing – review & editing. **Morgan A. Schake**: Formal analysis, Writing – review & editing. **Justin R. Brooks**: Methodology, Writing – review & editing. **Ruiguo Yang**: Methodology, Resources, Writing – review & editing. **Peter D. Weinberg**: Conceptualization, Resources, Writing – review & editing. **Ryan M. Pedrigi**: Conceptualization, Software, Formal analysis, Resources, Writing – original draft, Writing – review & editing, Visualization, Supervision, Project administration, Funding acquisition.

Declaration of Competing Interest

The authors declare that they have no known competing financial interests or personal relationships that could have appeared to influence the work reported in this paper.

Acknowledgements

This work was supported by the American Heart Association (19CDA34660218), the National Institute of Biomedical Imaging and Bioengineering of the National Institutes of Health

(R21EB028960), and the National Science Foundation (CMMI-1944131) to RMP. Manufacturing of the device to extract RNA from different portions of the culture plate and confocal imaging were performed at the NanoEngineering Research Core Facility (NERCF), which is partially funded by the Nebraska Research Initiative.

References

Anno, T., Sakamoto, N., Sato, M., 2012. Role of nesprin-1 in nuclear deformation in endothelial cells under static and uniaxial stretching conditions. Biochem Biophys Res Commun 424, 94-99. https://doi.org/10.1016/j.bbrc.2012.06.073

Arshad, M., Ghim, M., Mohamied, Y., Sherwin, S.J., Weinberg, P.D., 2021. Endothelial cells do not align with the mean wall shear stress vector. J R Soc Interface 18, 20200772. https://doi.org/10.1098/rsif.2020.0772

Bond, A.R., Ni, C.W., Jo, H., Weinberg, P.D., 2010. Intimal cushions and endothelial nuclear elongation around mouse aortic branches and their spatial correspondence with patterns of lipid deposition. Am J Physiol Heart Circ Physiol 298, H536-544. https://doi.org/10.1152/ajpheart.00917.2009

Chatzizisis, Y.S., Baker, A.B., Sukhova, G.K., Koskinas, K.C., Papafaklis, M.I., Beigel, R., Jonas, M., Coskun, A.U., Stone, B.V., Maynard, C., Shi, G.P., Libby, P., Feldman, C.L., Edelman, E.R., Stone, P.H., 2011. Augmented expression and activity of extracellular matrix-degrading enzymes in regions of low endothelial shear stress colocalize with coronary atheromata with thin fibrous caps in pigs. Circulation 123, 621-630. https://doi.org/10.1161/CIRCULATIONAHA.110.970038

Cheng, C., Tempel, D., van Haperen, R., van der Baan, A., Grosveld, F., Daemen, M.J., Krams, R., de Crom, R., 2006. Atherosclerotic lesion size and vulnerability are determined by patterns of fluid shear stress. Circulation 113, 2744-2753. https://doi.org/10.1161/CIRCULATIONAHA.105.590018

Danielsson, B.E., Peters, H.C., Bathula, K., Spear, L.M., Noll, N.A., Dahl, K.N., Conway, D.E., 2022. Progerin-expressing endothelial cells are unable to adapt to shear stress. Biophys J 121, 620-628. https://doi.org/10.1016/j.bpj.2022.01.004

Davies, P.F., Civelek, M., Fang, Y., Fleming, I., 2013. The atherosusceptible endothelium: endothelial phenotypes in complex haemodynamic shear stress regions in vivo. Cardiovasc Res 99, 315-327. https://doi.org/10.1093/cvr/cvt101

Duerrschmidt, N., Stielow, C., Muller, G., Pagano, P.J., Morawietz, H., 2006. NO-mediated regulation of NAD(P)H oxidase by laminar shear stress in human endothelial cells. J Physiol 576, 557-567. https://doi.org/10.1113/jphysiol.2006.111070

Fedorchak, G.R., Kaminski, A., Lammerding, J., 2014. Cellular mechanosensing: getting to the nucleus of it all. Prog Biophys Mol Biol 115, 76-92. https://doi.org/10.1016/j.pbiomolbio.2014.06.009

Fledderus, J.O., Boon, R.A., Volger, O.L., Hurttila, H., Yla-Herttuala, S., Pannekoek, H., Levonen, A.L., Horrevoets, A.J., 2008. KLF2 primes the antioxidant transcription factor Nrf2 for activation in endothelial cells. Arterioscler Thromb Vasc Biol 28, 1339-1346. https://doi.org/10.1161/ATVBAHA.108.165811

Frangos, J.A., Eskin, S.G., McIntire, L.V., Ives, C.L., 1985. Flow effects on prostacyclin production by cultured human endothelial cells. Science 227, 1477-1479. https://doi.org/10.1126/science.3883488

Frueh, J., Maimari, N., Homma, T., Bovens, S.M., Pedrigi, R.M., Towhidi, L., Krams, R., 2013. Systems biology of the functional and dysfunctional endothelium. Cardiovasc Res 99, 334-341. https://doi.org/10.1093/cvr/cvt108

Ghim, M., Pang, K.T., Arshad, M., Wang, X., Weinberg, P.D., 2018. A novel method for segmenting growth of cells in sheared endothelial culture reveals the secretion of an anti-inflammatory mediator. J Biol Eng 12, 15. https://doi.org/10.1186/s13036-018-0107-6

Gijsen, F., Katagiri, Y., Barlis, P., Bourantas, C., Collet, C., Coskun, U., Daemen, J., Dijkstra, J., Edelman, E., Evans, P., van der Heiden, K., Hose, R., Koo, B.K., Krams, R., Marsden, A., Migliavacca, F., Onuma, Y., Ooi, A., Poon, E., Samady, H., Stone, P., Takahashi, K., Tang, D., Thondapu, V., Tenekecioglu, E., Timmins, L., Torii, R., Wentzel, J., Serruys, P., 2019. Expert recommendations on the assessment of wall shear stress in human coronary arteries: existing methodologies, technical considerations, and clinical applications. Eur Heart J 40, 3421-3433. https://doi.org/10.1093/eurheartj/ehz551

Hoogendoorn, A., Kok, A.M., Hartman, E.M.J., de Nisco, G., Casadonte, L., Chiastra, C., Coenen, A., Korteland, S.A., Van der Heiden, K., Gijsen, F.J.H., Duncker, D.J., van der Steen, A.F.W., Wentzel, J.J., 2020. Multidirectional wall shear stress promotes advanced coronary plaque development: comparing five shear stress metrics. Cardiovasc Res 116, 1136-1146. https://doi.org/10.1093/cvr/cvz212

Hosoya, T., Maruyama, A., Kang, M.I., Kawatani, Y., Shibata, T., Uchida, K., Warabi, E., Noguchi, N., Itoh, K., Yamamoto, M., 2005. Differential responses of the Nrf2-Keap1 system to laminar and oscillatory shear stresses in endothelial cells. J Biol Chem 280, 27244-27250. https://doi.org/10.1074/jbc.M502551200

Humphrey, J.D., 2008. Mechanisms of arterial remodeling in hypertension: coupled roles of wall shear and intramural stress. Hypertension 52, 195-200. https://doi.org/10.1161/HYPERTENSIONAHA.107.103440

Jin, Y.J., Chennupati, R., Li, R., Liang, G., Wang, S., Iring, A., Graumann, J., Wettschureck, N., Offermanns, S., 2021. Protein kinase N2 mediates flow-induced eNOS activation and vascular tone regulation. J Clin Invest. https://doi.org/10.1172/JCI145734

Kok, A.M., Molony, D.S., Timmins, L.H., Ko, Y.A., Boersma, E., Eshtehardi, P., Wentzel, J.J., Samady, H., 2019. The influence of multidirectional shear stress on plaque progression and composition changes in human coronary arteries. EuroIntervention 15, 692-699. https://doi.org/10.4244/EIJ-D-18-00529

Mammoto, A., Mammoto, T., Ingber, D.E., 2012. Mechanosensitive mechanisms in transcriptional regulation. J Cell Sci 125, 3061-3073. https://doi.org/10.1242/jcs.093005

Maurya, M.R., Gupta, S., Li, J.Y., Ajami, N.E., Chen, Z.B., Shyy, J.Y., Chien, S., Subramaniam, S., 2021. Longitudinal shear stress response in human endothelial cells to atheroprone and atheroprotective conditions. Proc Natl Acad Sci U S A 118. https://doi.org/10.1073/pnas.2023236118

McCormick, S.M., Eskin, S.G., McIntire, L.V., Teng, C.L., Lu, C.M., Russell, C.G., Chittur, K.K., 2001. DNA microarray reveals changes in gene expression of shear stressed human umbilical vein endothelial cells. Proc Natl Acad Sci U S A 98, 8955-8960. https://doi.org/10.1073/pnas.171259298

Miller, H.A., Schake, M.A., Bony, B.A., Curtis, E.T., Gee, C.C., McCue, I.S., Ripperda, T.J., Jr., Chatzizisis, Y.S., Kievit, F.M., Pedrigi, R.M., 2021. Smooth muscle cells affect differential nanoparticle accumulation in disturbed blood flow-induced murine atherosclerosis. PLoS One 16, e0260606. https://doi.org/10.1371/journal.pone.0260606

Mohamied, Y., Rowland, E.M., Bailey, E.L., Sherwin, S.J., Schwartz, M.A., Weinberg, P.D., 2015. Change of direction in the biomechanics of atherosclerosis. Ann Biomed Eng 43, 16-25. https://doi.org/10.1007/s10439-014-1095-4

Mukaka, M.M., 2012. Statistics corner: A guide to appropriate use of correlation coefficient in medical research. Malawi Med J 24, 69-71.

Noris, M., Morigi, M., Donadelli, R., Aiello, S., Foppolo, M., Todeschini, M., Orisio, S., Remuzzi, G., Remuzzi, A., 1995. Nitric oxide synthesis by cultured endothelial cells is modulated by flow conditions. Circ Res 76, 536-543. https://doi.org/10.1161/01.res.76.4.536

Okamoto, T., Okabe, S., 2000. Ultraviolet absorbance at 260 and 280 nm in RNA measurement is dependent on measurement solution. Int J Mol Med 5, 657-659. https://doi.org/10.3892/ijmm.5.6.657

Pedrigi, R.M., Mehta, V.V., Bovens, S.M., Mohri, Z., Poulsen, C.B., Gsell, W., Tremoleda, J.L., Towhidi, L., de Silva, R., Petretto, E., Krams, R., 2016. Influence of shear stress magnitude and direction on atherosclerotic plaque composition. R Soc Open Sci 3, 160588. https://doi.org/10.1098/rsos.160588

Pedrigi, R.M., Poulsen, C.B., Mehta, V.V., Ramsing Holm, N., Pareek, N., Post, A.L., Kilic, I.D., Banya, W.A., Dall'Ara, G., Mattesini, A., Bjorklund, M.M., Andersen, N.P., Grondal, A.K., Petretto, E., Foin, N., Davies, J.E., Di Mario, C., Fog Bentzon, J., Erik Botker, H., Falk, E., Krams, R., de Silva, R., 2015. Inducing Persistent Flow Disturbances Accelerates Atherogenesis and Promotes Thin Cap Fibroatheroma Development in D374Y-PCSK9 Hypercholesterolemic Minipigs. Circulation 132, 1003-1012. https://doi.org/10.1161/CIRCULATIONAHA.115.016270

Peghaire, C., Dufton, N.P., Lang, M., Salles, C., II, Ahnstrom, J., Kalna, V., Raimondi, C., Pericleous, C., Inuabasi, L., Kiseleva, R., Muzykantov, V.R., Mason, J.C., Birdsey, G.M., Randi, A.M., 2019. The transcription factor ERG regulates a low shear stress-induced anti-thrombotic pathway in the microvasculature. Nat Commun 10, 5014. https://doi.org/10.1038/s41467-019-12897-w

Peiffer, V., Sherwin, S.J., Weinberg, P.D., 2013. Computation in the rabbit aorta of a new metric - the transverse wall shear stress - to quantify the multidirectional character of disturbed blood flow. J Biomech 46, 2651-2658. https://doi.org/10.1016/j.jbiomech.2013.08.003

Rizzo, V., Morton, C., DePaola, N., Schnitzer, J.E., Davies, P.F., 2003. Recruitment of endothelial caveolae into mechanotransduction pathways by flow conditioning in vitro. Am J Physiol Heart Circ Physiol 285, H1720-1729. https://doi.org/10.1152/ajpheart.00344.2002

Samady, H., Eshtehardi, P., McDaniel, M.C., Suo, J., Dhawan, S.S., Maynard, C., Timmins, L.H., Quyyumi, A.A., Giddens, D.P., 2011. Coronary artery wall shear stress is associated with progression and transformation of atherosclerotic plaque and arterial remodeling in patients with coronary artery disease. Circulation 124, 779-788. https://doi.org/10.1161/CIRCULATIONAHA.111.021824

Schneider, C.A., Rasband, W.S., Eliceiri, K.W., 2012. NIH Image to ImageJ: 25 years of image analysis. Nat Methods 9, 671-675. https://doi.org/10.1038/nmeth.2089

Siu, K.L., Gao, L., Cai, H., 2016. Differential Roles of Protein Complexes NOX1-NOXO1 and NOX2-p47phox in Mediating Endothelial Redox Responses to Oscillatory and Unidirectional Laminar Shear Stress. J Biol Chem 291, 8653-8662. https://doi.org/10.1074/jbc.M115.713149

Stone, P.H., Maehara, A., Coskun, A.U., Maynard, C.C., Zaromytidou, M., Siasos, G., Andreou, I., Fotiadis, D., Stefanou, K., Papafaklis, M., Michalis, L., Lansky, A.J., Mintz, G.S., Serruys, P.W., Feldman, C.L., Stone, G.W., 2018. Role of Low Endothelial Shear Stress and Plaque Characteristics in the Prediction of Nonculprit Major Adverse Cardiac Events: The PROSPECT Study. JACC Cardiovasc Imaging 11, 462-471. https://doi.org/10.1016/j.jcmg.2017.01.031

Stone, P.H., Saito, S., Takahashi, S., Makita, Y., Nakamura, S., Kawasaki, T., Takahashi, A., Katsuki, T., Nakamura, S., Namiki, A., Hirohata, A., Matsumura, T., Yamazaki, S., Yokoi, H., Tanaka, S., Otsuji, S., Yoshimachi, F., Honye, J., Harwood, D., Reitman, M., Coskun, A.U., Papafaklis, M.I., Feldman, C.L., Investigators, P., 2012. Prediction of progression of coronary artery disease and clinical outcomes using vascular profiling of endothelial shear

stress and arterial plaque characteristics: the PREDICTION Study. Circulation 126, 172-181. https://doi.org/10.1161/CIRCULATIONAHA.112.096438

Timmins, L.H., Molony, D.S., Eshtehardi, P., McDaniel, M.C., Oshinski, J.N., Giddens, D.P., Samady, H., 2017. Oscillatory wall shear stress is a dominant flow characteristic affecting lesion progression patterns and plaque vulnerability in patients with coronary artery disease. J R Soc Interface 14. https://doi.org/10.1098/rsif.2016.0972

Walsh, T.G., Murphy, R.P., Fitzpatrick, P., Rochfort, K.D., Guinan, A.F., Murphy, A., Cummins, P.M., 2011. Stabilization of brain microvascular endothelial barrier function by shear stress involves VE-cadherin signaling leading to modulation of pTyr-occludin levels. J Cell Physiol 226, 3053-3063. https://doi.org/10.1002/jcp.22655

Warboys, C.M., de Luca, A., Amini, N., Luong, L., Duckles, H., Hsiao, S., White, A., Biswas, S., Khamis, R., Chong, C.K., Cheung, W.M., Sherwin, S.J., Bennett, M.R., Gil, J., Mason, J.C., Haskard, D.O., Evans, P.C., 2014. Disturbed flow promotes endothelial senescence via a p53-dependent pathway. Arterioscler Thromb Vasc Biol 34, 985-995. https://doi.org/10.1161/ATVBAHA.114.303415

Warboys, C.M., Ghim, M., Weinberg, P.D., 2019. Understanding mechanobiology in cultured endothelium: A review of the orbital shaker method. Atherosclerosis 285, 170-177. https://doi.org/10.1016/j.atherosclerosis.2019.04.210

Won, D., Zhu, S.N., Chen, M., Teichert, A.M., Fish, J.E., Matouk, C.C., Bonert, M., Ojha, M., Marsden, P.A., Cybulsky, M.I., 2007. Relative reduction of endothelial nitric-oxide synthase expression and transcription in atherosclerosis-prone regions of the mouse aorta and in an in vitro model of disturbed flow. Am J Pathol 171, 1691-1704. https://doi.org/10.2353/ajpath.2007.060860

A

B

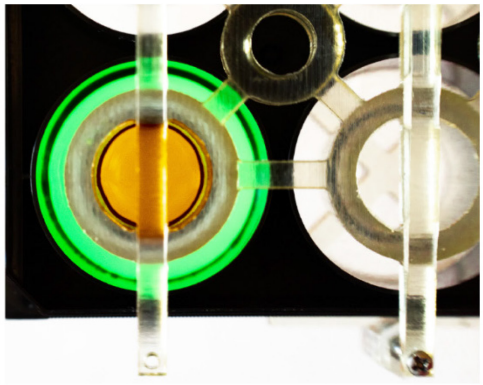

C

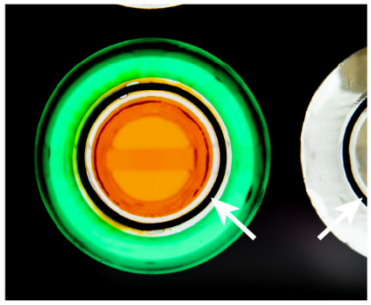

Figure 1. Custom 3-D printed mask used to separate the center and periphery of each well of a culture plate for extraction of RNA. (A) The entire mask attached (via screws at the midpoint) to a baseplate that secured it to a 6-well culture plate. (B) Top view of an example well with dye-colored water to illustrate the efficacy of the mask in separating the solution in the central portion (orange) from the outer portion (green). (C) Underside of one well (and partial of another) showing the separation of the two regions via a silicon gasket (arrows).

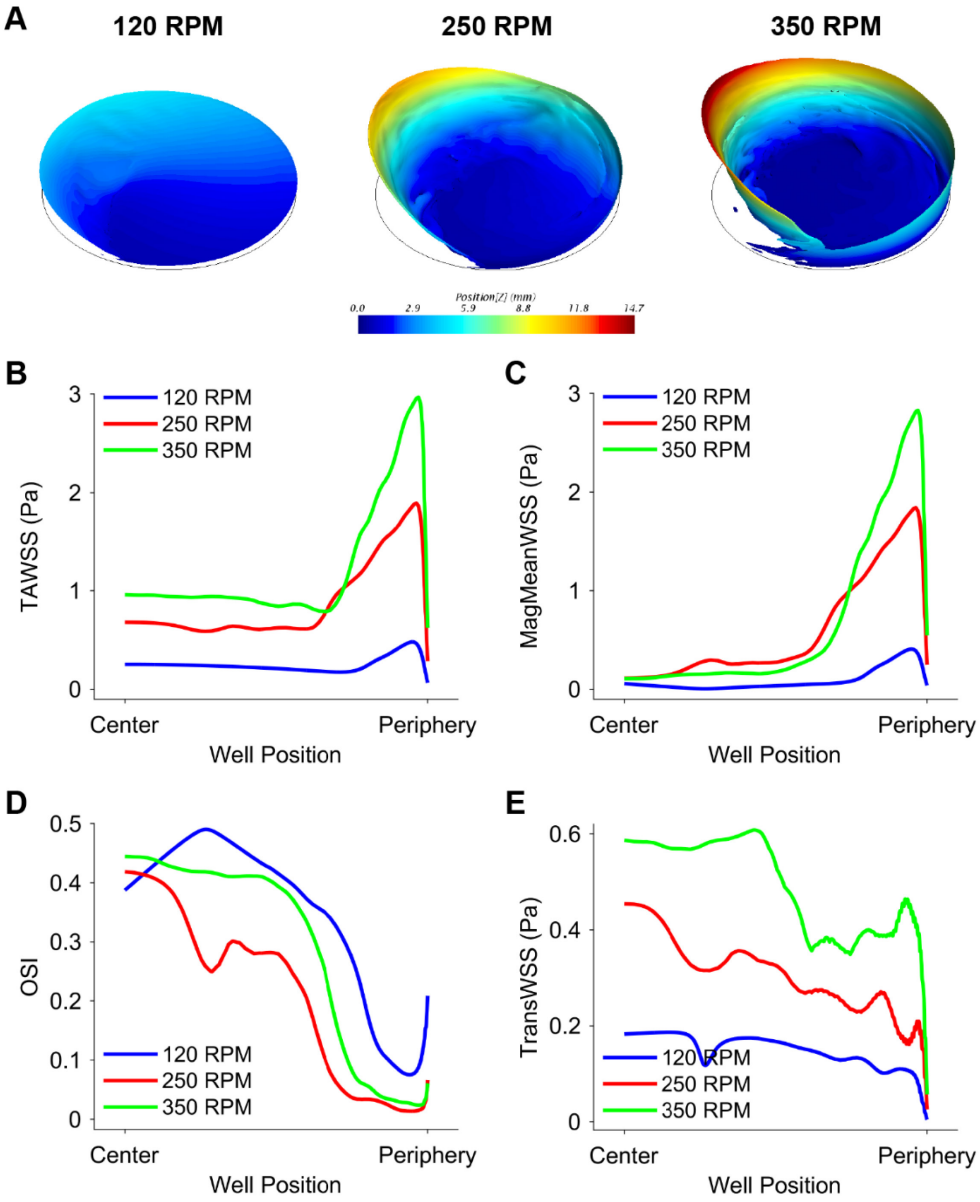

Figure 2. CFD simulations of swirling media and associated shear stress metrics in a culture plate well under orbital flow. (A) Simulations at 120, 250, and 350 RPM where color map and scale bar indicate fluid height. (B-E) Shear metrics calculated from the center to periphery of the well in each CFD model at each angular velocity, including (B) TAWSS, (C) MagMeanWSS, (D) OSI, and (E) TransWSS.

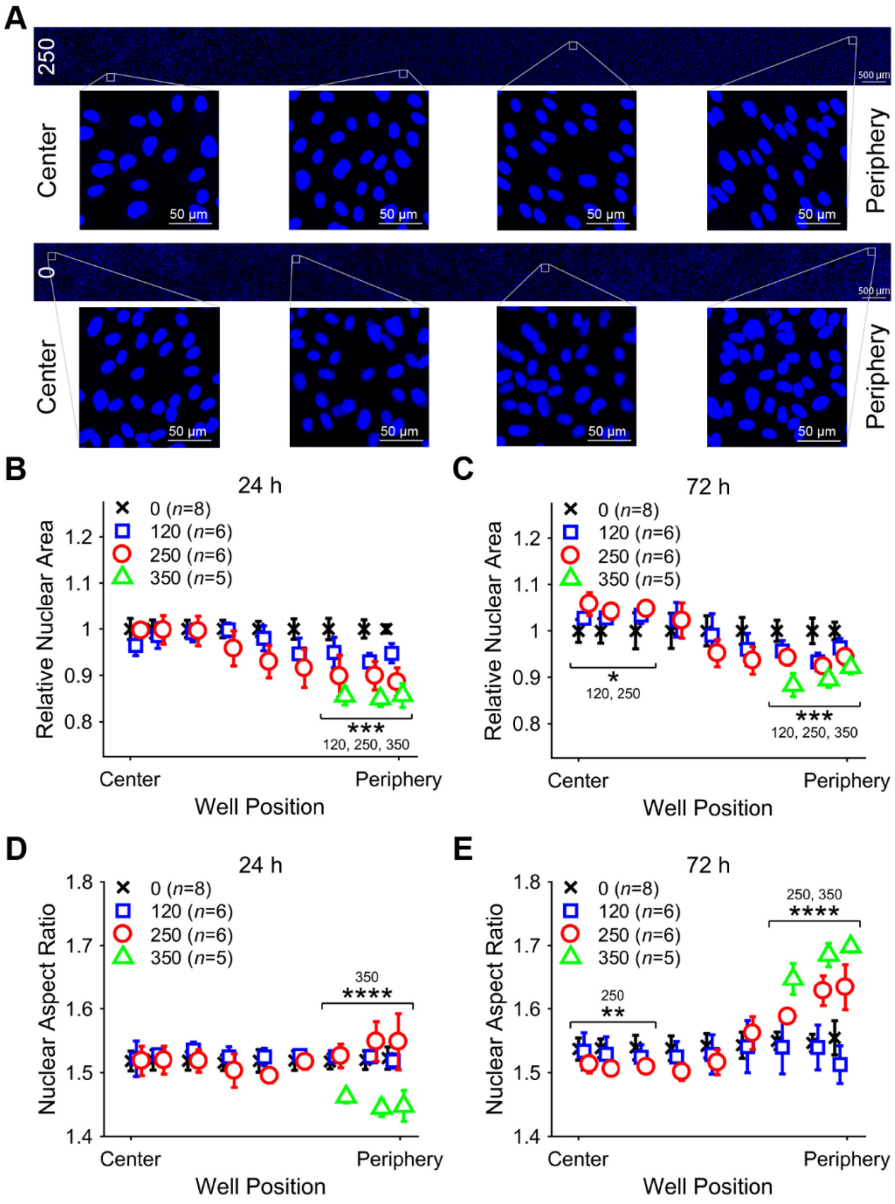

Figure 3. Endothelial nuclear morphology under orbital flow as a function of radial position in the well. (A) Confocal tile scans of DAPI from the center to the periphery of a representative cell layer after orbital flow at 250 and 0 (static control) RPM for 72 h with representative high magnification images at select locations. (B-C) Plots of nuclear area relative to the mean of static controls over the radius of each well from center to periphery at (B) 24 h and (C) 72 h. (D-E) Plots of nuclear aspect ratio over the radius of each well from center to periphery at (D) 24 h and (E) 72 h. Data from controls (0 RPM) are shown at the exact well position, whereas other data are slightly staggered to improve clarity. The *n* refers to the number of cell layers assessed for each orbital velocity (in RPM). Data are mean ± SD. *Indicates statistically significant difference (p<0.05) compared to static controls.

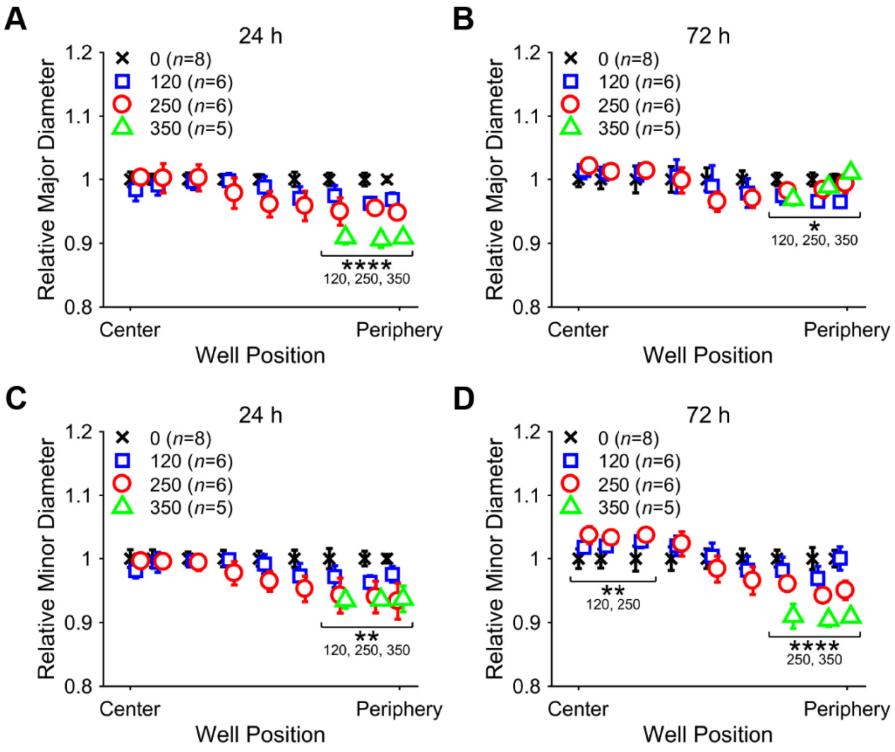

Figure 4. Endothelial nuclear major and minor diameters under orbital flow as a function of radial position in the well. (A-B) Plots of nuclear major diameter relative to the mean of static controls over the radius of each well from center to periphery at (A) 24 h and (B) 72 h. (C-D) Plots of nuclear minor diameter over the radius of each well from center to periphery at (C) 24 h and (D) 72 h. Data from controls (0 RPM) are shown at the exact well position, whereas other data are slightly staggered to improve clarity. The *n* refers to the number of cell layers assessed for each orbital velocity (in RPM). Data are mean ± SD. *Indicates a statistically significant difference ($p<0.05$) compared to static controls.

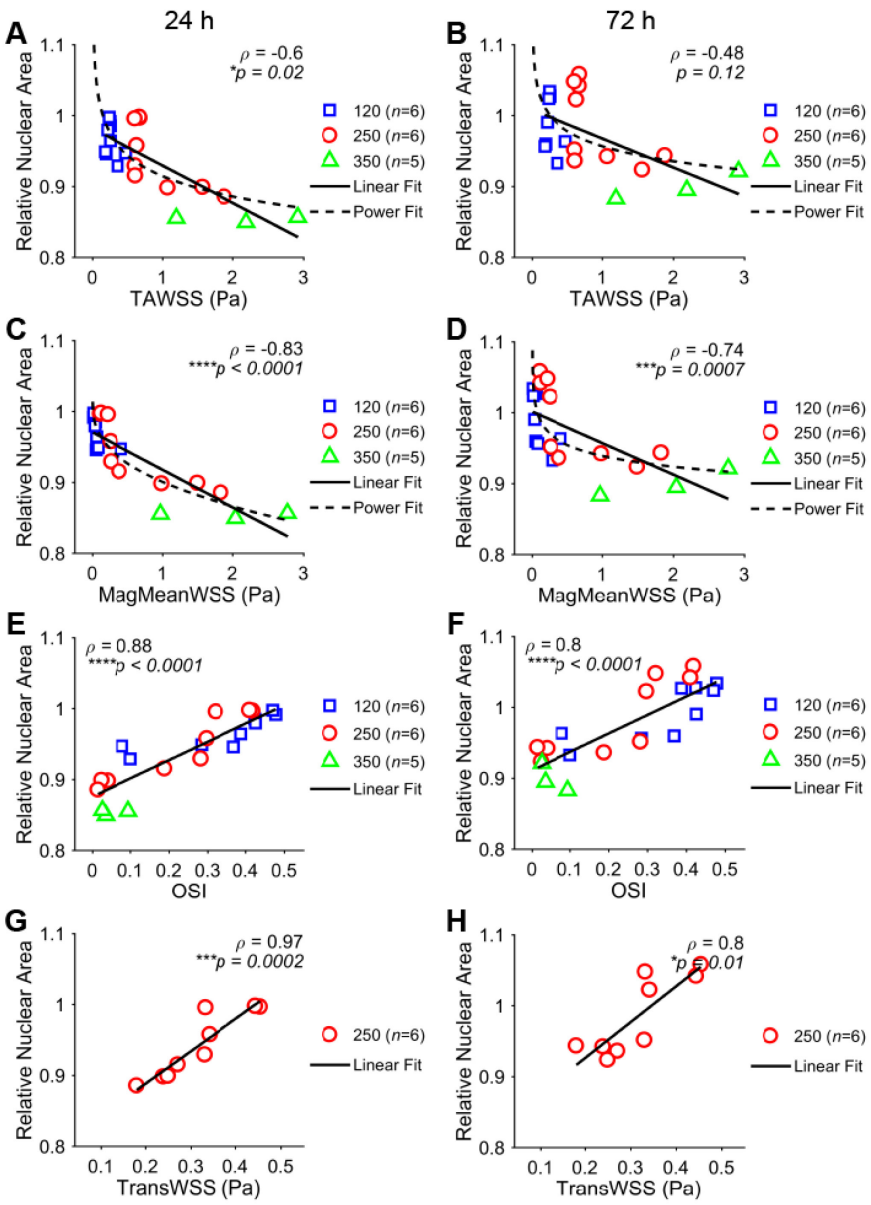

Figure 5. Endothelial nuclear area as a function of the WSS metrics. (A-H) Plots of nuclear area (relative to the mean of static controls) versus each WSS metric, including (A-B) TAWSS, (C-D) MagMeanWSS, (E-F) OSI, and (G-H) TransWSS at (column 1) 24 h and (column 2) 72 h. Data points were averaged over all cell layers (indicated by *n*) for each orbital velocity (120, 250, and 350 RPM) at each duration and radial position in the well (multiple data points for an orbital velocity represent the multiple radial locations assessed for the cell layers; TransWSS was only assessed at 250 RPM due to inconsistencies in the data between orbital velocities). The black line represents a best-fit line (solid) and, in some cases, power (dashed) function across all data points to visualize the trend. The Spearman's correlation coefficient (ρ) and associated *p*-value are given for each plot. *$p<0.05$ is considered statistically significant.

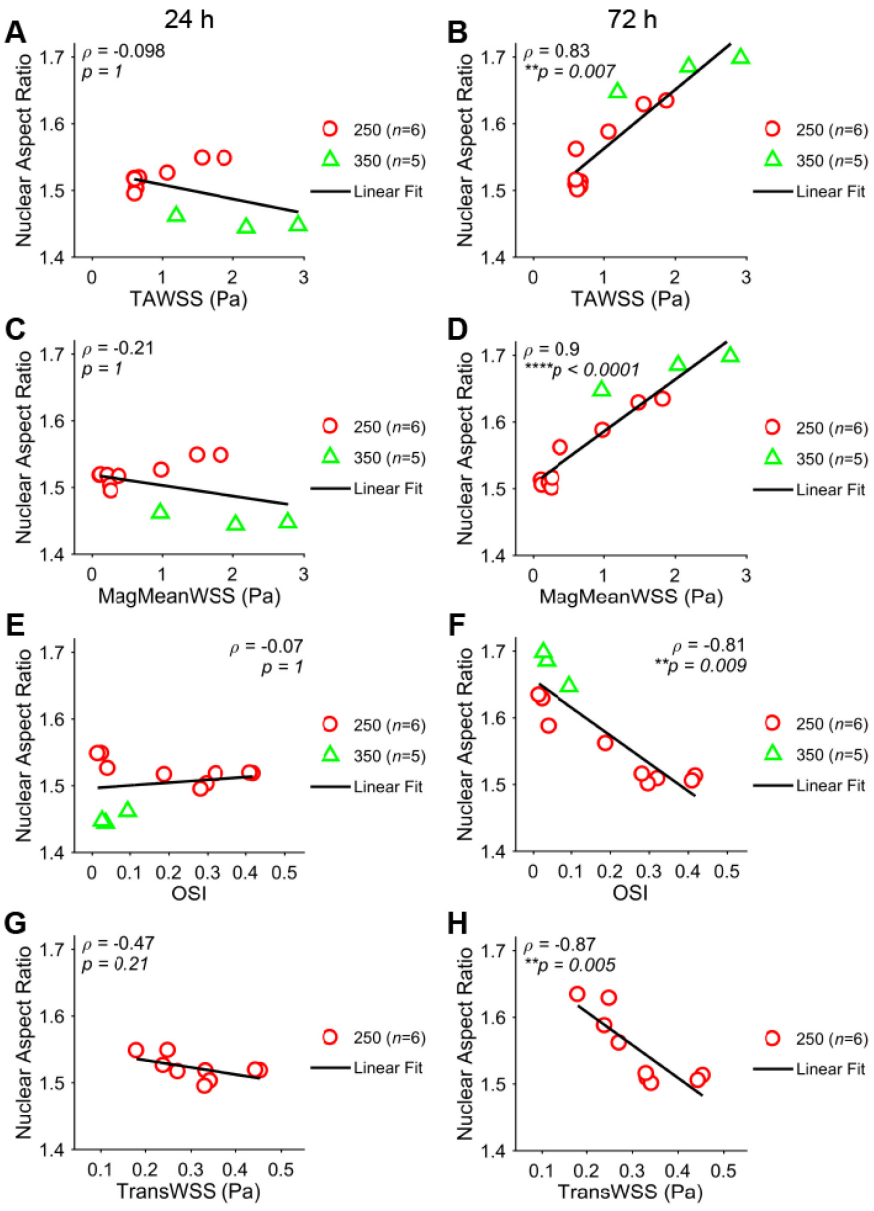

Figure 6. Endothelial nuclear aspect ratio as a function of the WSS metrics. (A-H) Plots of nuclear aspect ratio versus each WSS metric, including (A-B) TAWSS, (C-D) MagMeanWSS, (E-F) OSI, and (G-H) TransWSS at (column 1) 24 h and (column 2) 72 h. Data points were averaged over all cell layers (indicated by *n*) for each orbital velocity (250 and 350 RPM) at each duration and radial position in the well (multiple data points for an orbital velocity represent the multiple radial locations assessed for the cell layers; TransWSS was only assessed at 250 RPM due to inconsistencies in the data between orbital velocities). The black line represents a linear regression of all data points to visualize the trend. The Spearman's correlation coefficient (ρ) and associated *p*-value are given for each plot. *p<0.05 is considered statistically significant.

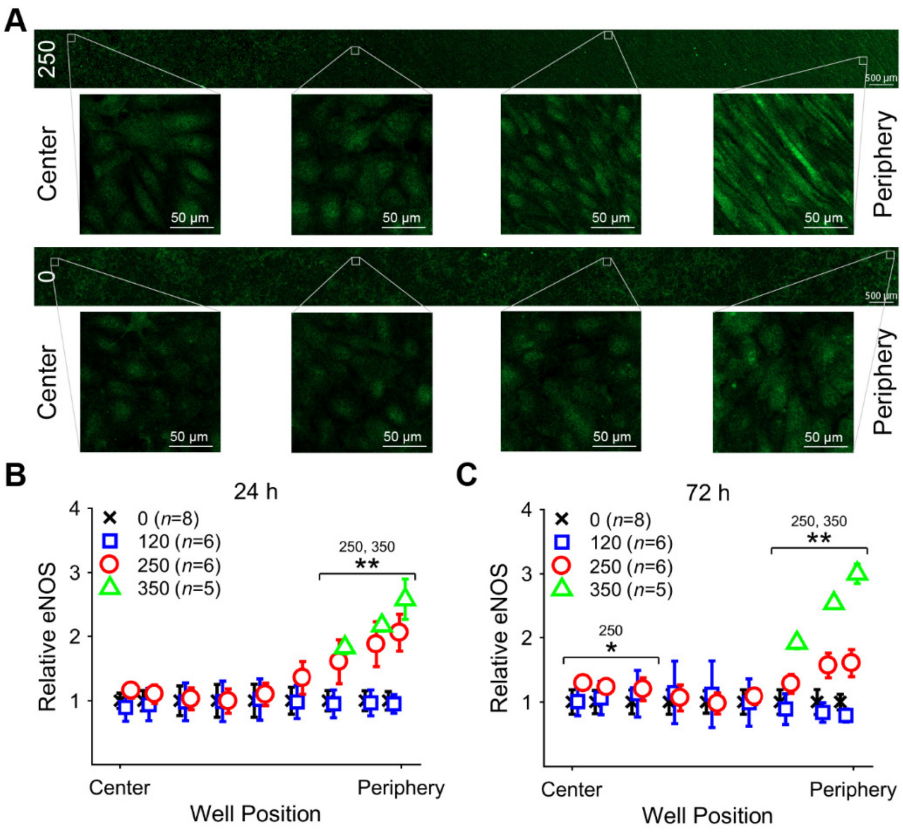

Figure 7. Endothelial expression of eNOS under orbital flow as a function of radial position in the well. (A) Confocal tile scans of eNOS from the center to the periphery of a representative cell layer after orbital flow at 250 and 0 (static control) RPM for 72 h with representative high magnification images at select locations. (B-C) Plots of eNOS relative to the mean of static controls over the radius of each well from center to periphery at (B) 24 h and (C) 72 h. Data from controls (0 RPM) are shown at the exact well position, whereas other data are slightly staggered to improve clarity. The *n* refers to the number of cell layers assessed for each orbital velocity (in RPM). Data are mean ± SD. *Indicates statistically significant difference (p<0.05) compared to static controls.

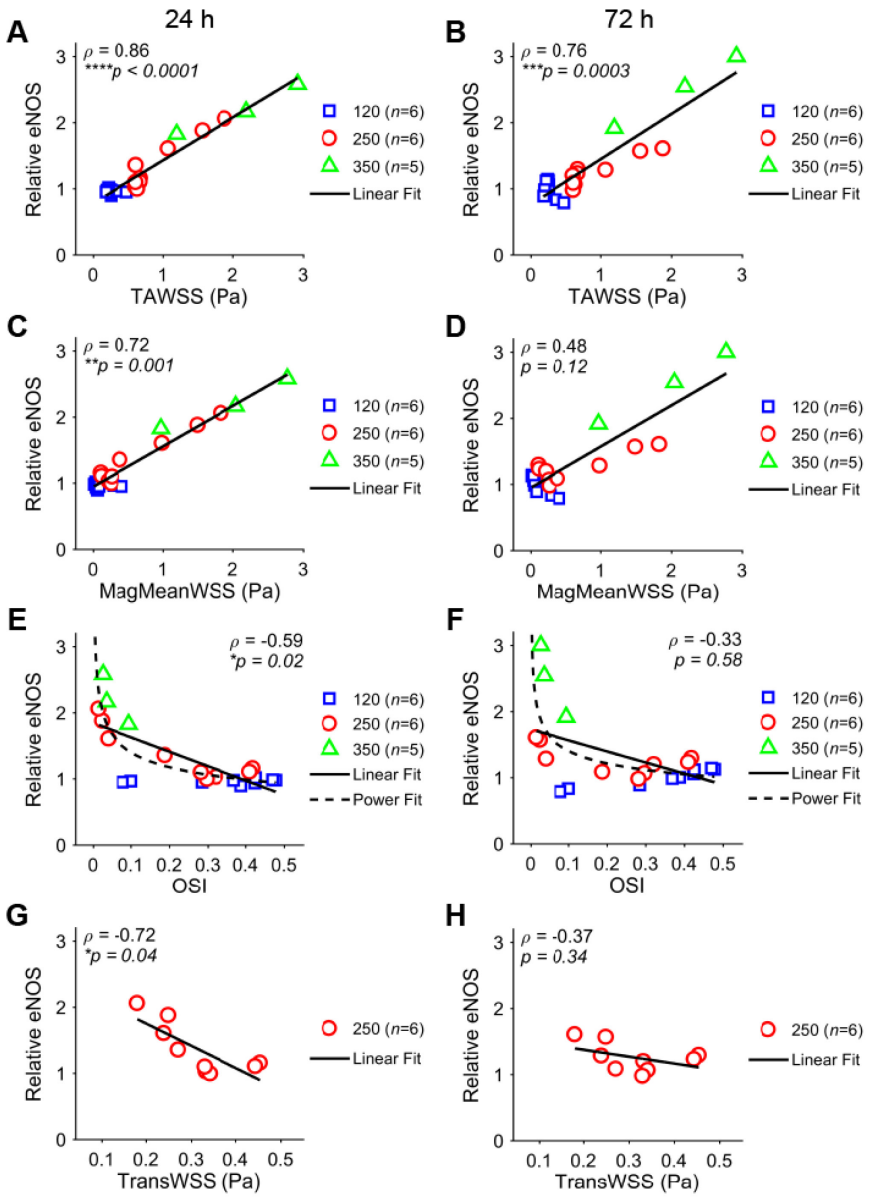

Figure 8. Endothelial eNOS expression as a function of the WSS metrics. (A-H) Plots of eNOS (relative to the mean of static controls) versus each WSS metric, including (A-B) TAWSS, (C-D) MagMeanWSS, (E-F) OSI, and (G-H) TransWSS at (column 1) 24 h and (column 2) 72 h. Data points were averaged over all cell layers (indicated by *n*) for each orbital velocity (120, 250, and 350 RPM) at each duration and radial position in the well (multiple data points for an orbital velocity represent the multiple radial locations assessed for the cell layers; TransWSS was only assessed at 250 RPM due to inconsistencies in the data between orbital velocities). The black line represents a best-fit line (solid) and, in some cases, power (dashed) function across all data points to visualize the trend. The Spearman's correlation coefficient (ρ) and associated *p*-value are given for each plot. *p<0.05 is considered statistically significant.

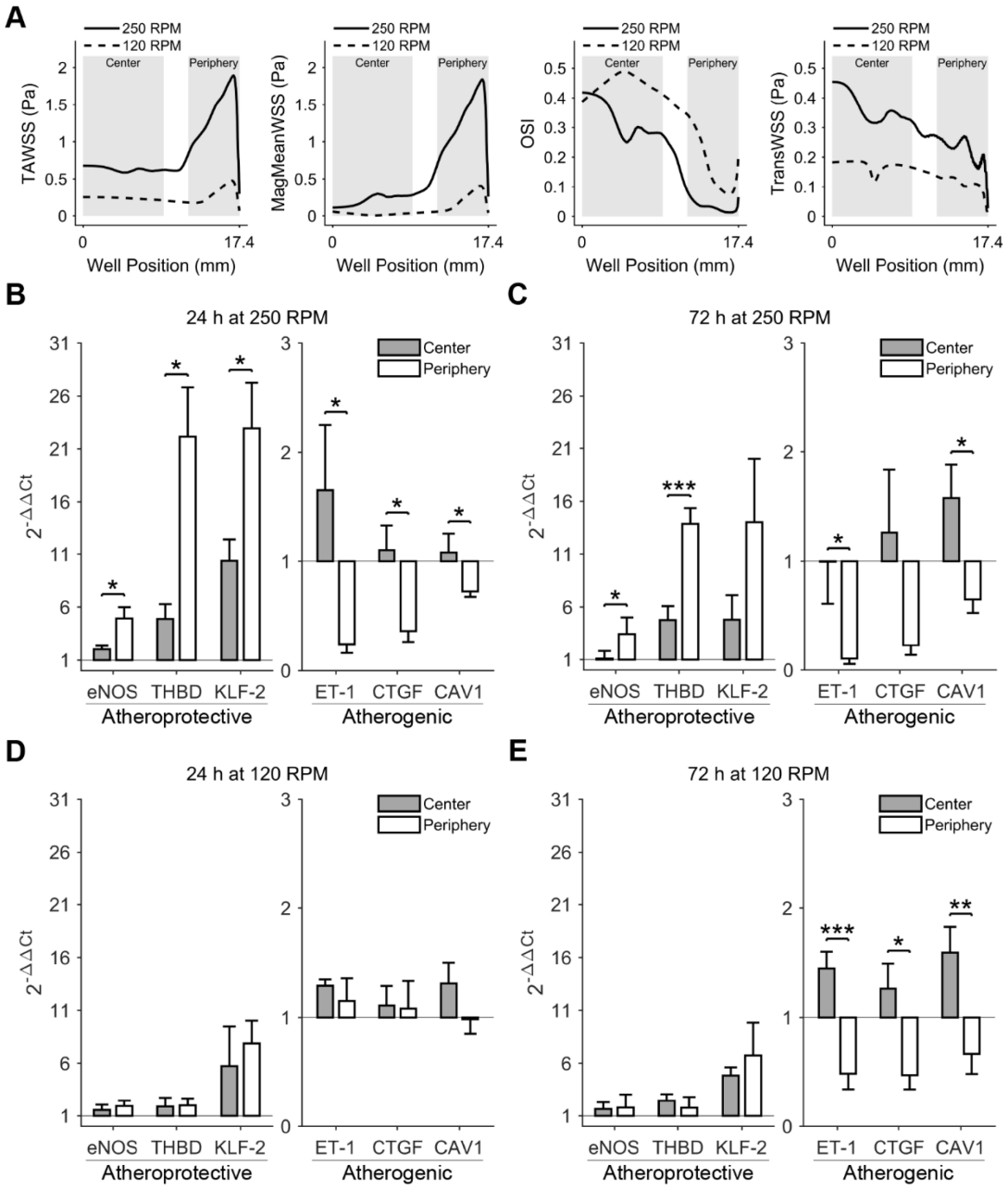

Figure 9. Expression of atheroprotective and atherogenic genes at the center and periphery of endothelial cell layers under orbital flow as assessed by RT-qPCR. (A) Shear metric patterns at 250 (solid line) and 120 (dotted line) RPM in the center and periphery regions of each well where RNA was extracted. Gene expression at the center (grey bars) and periphery (white bars) of wells under orbital flow for (B) 24 h at 250 RPM, (C) 72 h at 250 RPM, (D) 24 h at 120 RPM, and (E) 72 h at 120 RPM. Data are mean ± SD and averaged over n=5 cell layers per condition. *p<0.05 is considered statistically significant. Note, the y-axis is scaled differently for the atheroprotective and atherogenic genes to better show differences between center and periphery for all genes.